1. Large Helical Device (LHD) Project

The Large Helical Device (LHD) project conducts fusion-grade confinement research in a steady-state machine to elucidate important research issues in physics and engineering for the helical-type fusion reactor.

The LHD is one of the largest helical devices, with major and averaged minor radii of 3.6 – 4.0 m and 0.6 m, respectively. A double helical coil and three pairs of poloidal coils are all superconducting, by which maximum magnetic field strength at the plasma center is 3 T. For plasma heating, three negative-ion-based 180 – 190 keV neutral beams with total heating power of 8 – 16 MW are injected tangentially to the plasma.

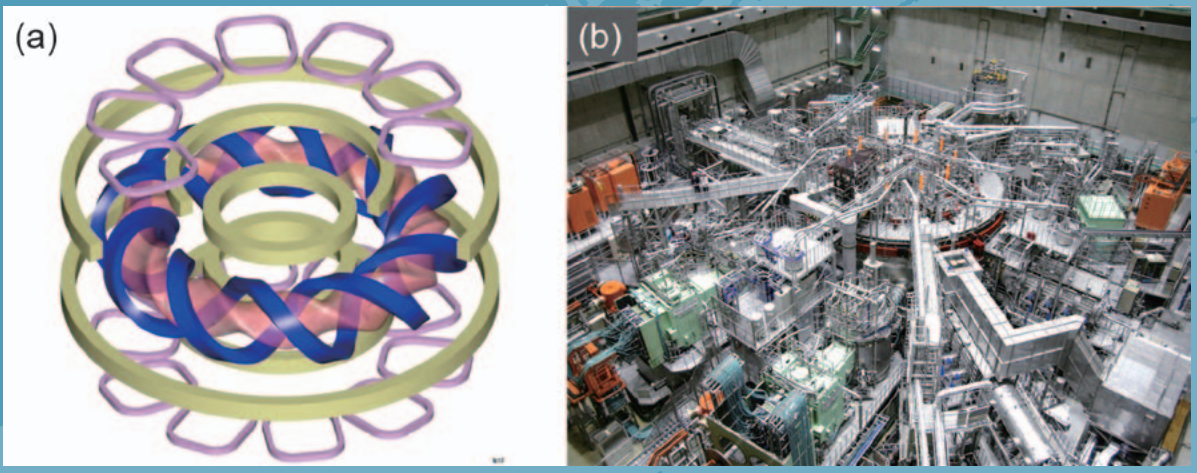

Fig. 1 (a) Coil configuration of LHD. Superconducting helical coils (blue), poloidal coils (yellow) and normal conducting RMP coils, together with plasma. (b) LHD torus hall.

Two positive-ion-based 40 – 80 keV neutral beams with total heating power of 6 – 18 MW are also injected perpendicular to the plasma. In addition, electron cyclotron resonance heating with total heating power of ~ 5.5 MW is also available. For fuelling, LHD is equipped with four gas puff valves and two pellet injectors.

Since 2018, LHD has performed the deuterium experiment in which plasma is expected to improve its performance, thanks to the "isotope effect". Achieved plasma parameters to date are summarized in Table 1.

Table 1 A Achieved plasma parameters (1990 – 2018)

Parameters	Achieved	Key physics	Target
T_i	10 keV ($n_e = 1.3\times10^{19}$ m^{-3})	Ion ITB Impurity hole	10 keV ($n_e = 2\times10^{19}$m^{-3})
T_e	20 keV (2×10^{18} m^{-3}) 10 keV (1.6×10^{19} m^{-3})	Electron ITB	10 keV (2×10^{19}m^{-3})
Density	1.2×10^{21}m^{-3} ($T_e = 0.25$ keV)	Super dense core	4×10^{20} m^{-3} ($T_e = 1.3$ keV)
β	5.1 % ($B_T = 0.425$ T) 4.1 % (1 T)	MHD in current-free plasmas	5 % ($B_T = 1$ - 2 T)
Steady-state operation	54min. 28sec (0.5MW, 1keV, 4×10^{18}m^{-3}) 47min. 39sec. (1.2MW, 2keV, 1×10^{19}m^{-3})	Dynamic wall retention	1 hour (3 MW)

(T. Morisaki)

High Performance Plasma

Highlight

Extension of high temperature operational regime

In future reactors, the fusion reaction is expected to be sustained under the electron heating dominant condition, where both the ion temperature (T_i) and the electron temperature (T_e) are high. Thus not only the investigation of the confinement improvement but also the characterization of the thermal transport for the plasmas, of which T_i and T_e are simultaneously high, are necessary. In the present status, such a plasma condition is realized by the combination heating of a neutral beam injection (NBI) and an electron cyclotron resonance heating (ECRH).

In the Large Helical Device (LHD), the deuterium (D) experiment was initiated in March 2017 in order to seek higher performance plasmas and to study the mechanism of the increased performance by isotope effect. In the first D experiment campaign in 2017, we successfully attained the T_i of 10 keV [1]. The achievement of the T_i value is a milestone toward realizing a helical reactor, which has an intrinsic advantage for steady state operation, because the T_i value is one of the important ignition conditions. In the FY2018 experimental campaign, we focused on the performance integration of high temperature plasmas and the investigation of confinement characteristics of plasmas, of which T_i and T_e is simultaneously high. As a representative result, high temperature operation regime could be successfully extended. The extended operation regime and the typical temperature and electron density (n_e) profiles are shown in Fig. 1 (a) and (b), respectively. The extended high temperature regime was realized due to the suppression of EIC (Energetic ion driven interchange) modes and the control of the T_e/T_i in the moderate range, where the ion thermal confinement does not degrade [2].

(H. Takahashi)

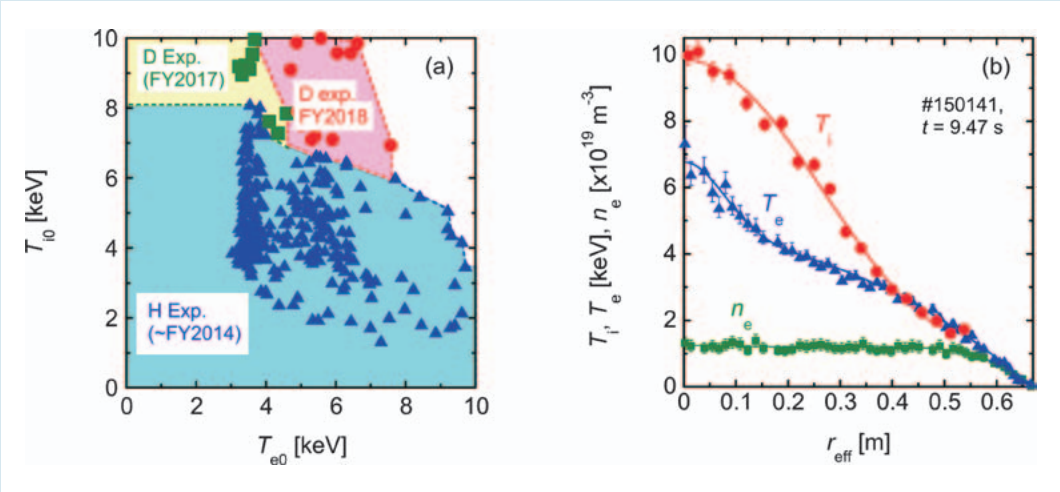

Fig. 1 (a) The operational map of high temperature plasmas, (b) the radial profiles of T_i, T_e, n_e of the typical plasma obtained in FY2018, of which T_i and T_e are simultaneously high [2].

Realization of higher ion temperature due to the suppression of EIC using ECRH

In the D experiments initiated in the LHD from 2017, the simultaneous high T_i and high T_e regime has been successfully extended mainly due to the suppression of the EIC modes and control of the T_e/T_i value. The EIC is triggered by helically trapped ions at lower order magnetic resonant surface and the EIC causes loss of high energy ions, leading to the decrease in T_i [3]. The mode width of EIC depends on $T_e^{-1/2}$ thus the increase in T_e at resonant surface is expected to be effective to suppress the EIC.

Figure 2 shows the comparison of the time evolution of (a) the heating power, (b) the line-averaged-electron density n_{e_fir}, (c) the poloidal magnetic fluctuation amplitude B_θ, (d) the neutron emission rate S_n, (e) the central electron temperature T_{e0}, (f) the central ion temperature T_{i0}, and the radial profiles of (g) the T_e and (h) the T_i in the plasmas which the highest T_i was achieved in the FY2017 and the 2018 experimental campaign. The NBI power was similar (~30 MW). The t_0 in the horizontal axis represents the plasma start-up timing. In the plasma obtained in FY2017, the EIC event occurred and the significant drop in the S_n was observed. This represents the loss of the high energy particles from the plasma. On the other hand, the EICs were clearly suppressed in #150133 using the superposed ECRH. Due to the suppression of the EICs, T_{i0} exceeded the previous record of 10 keV [2].

(H. Takahashi)

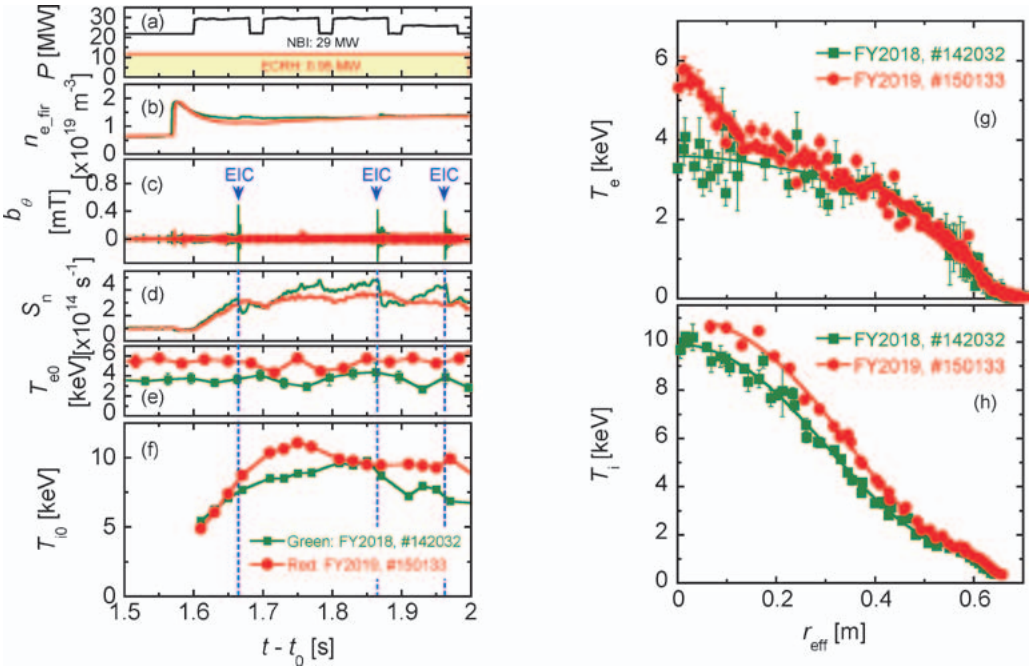

Fig. 2 Time evolution of (a) the heating power, (b) the line-averaged-electron density n_{e_fir}, (c) the poloidal magnetic fluctuation amplitude B_θ, (d) the neutron emission rate S_n, (e) the central electron temperature T_{e0}, (f) the central ion temperature T_{i0}, and the radial profiles of (g) the T_e and (h) the T_i in the plasmas which the highest T_i was achieved in the FY2017 and the 2018 experimental campaign [2].

Isotope effect in the internal transport barrier strength

In order to unveil the isotope effect in the internal transport barrier (ITB), a measure of the ITB strength newly defined. The ITB strength deuterium (D) and hydrogen (H) plasmas is compared, and it is found that the ITB strength is systematically high in D plasmas than H plasmas.

Unlike the case of tokamak plasmas, there is no generally accepted criterion for the ITB strength in stellarators/heliotrons. Here, a new criterion for the ITB strength is proposed by defining a unique scalar coefficient. The typical L-mode plasmas in LHD are characterized by the dome-shaped temperature profile with the diffusion coefficient being proportional to the temperature to the power of a factor α, i.e., $\chi \propto T^{\alpha}$, where $\alpha = 1$ is widely applicable. The reference L-mode profile $T_L^{ref}(r)$ is defined by extrapolating the edge temperature profile to the core according to the solution of the thermal diffusion equation with $\chi \propto T^{\alpha}$. By comparing the volume integral of $n_e(r)T_L^{ref}(r)$ with the electron kinetic stored energy, the profile gain factor $G_{1.0}$ is defined as a measure of the ITB strength [4] to be

$$G_{1.0} = \frac{\int_0^a n_e(r) T_i(r) V' dr}{\int_0^a n_e(r) T_i^{ref}(r) V' dr},$$

where V' is the radial derivative of the plasma volume and a is the plasma minor radius.

In LHD, the ITB in the ion temperature profile is typically formed when an intense neutral beam heating is applied to low electron density plasmas. Figure 3 compares the high and low electron density discharges in D plasmas. Symbols and curves correspond to the measured data and $T_L^{ref}(r)$, respectively. Stronger ion temperature ITB is formed in the low electron density plasma with $G_{1.0} \sim 1.47$ compared to the high electron density plasma with $G_{1.0} \sim 1.01$.

The proposed method is applied to both D and H discharges with the line averaged density scan in the shot-to-shot basis (fig. 4). When the line averaged density ($\bar{n}_e$) is high, $G_{1.0} \sim 1$ that corresponds to the L-mode, and decreasing $\bar{n}_e$ leads to a non-monotonic increase in $G_{1.0}$. Larger $G_{1.0}$ is routinely observed in D plasmas in $\bar{n}_e < 2\times10^{19}$ m^{-3} [5]. The isotope difference in the ITB strength is much distinguishable compared to the isotope difference in the confinement scaling [6].

Another dedicated set of experiments was performed to identify a slowing down MHD mode for triggering a collapse of the ITB in electron temperature profile. The ITB collapse event is observed in the neutral beam switching experiments, in which the core rotational transform profile is forced to be reversed or flattened by the toroidal return current. The mode radial width expands as the rotation frequency decays after its emergence. By this mode activity, the central electron temperature gradient is gradually

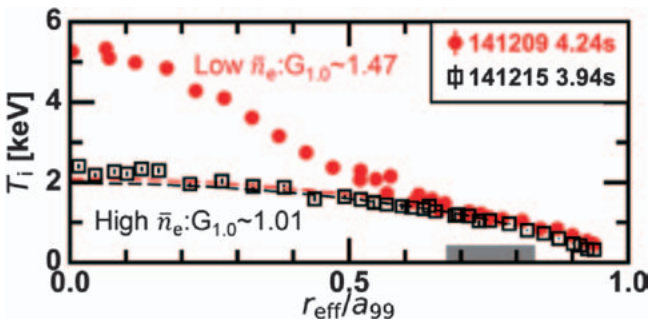

Fig. 3 Radial profiles of ion temperatures (symbols) and reference L-mode profiles (dashed curves) in low and high electron density discharges [5].

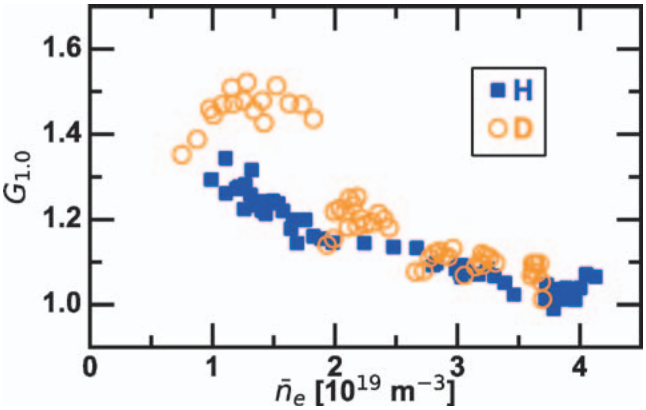

Fig. 4 Line averaged density dependence of the profile gain factor $G_{1.0}$ for D and H plasmas [5].

weakened. The mode is found to have two phase inversion points in radius, which we call the double-odd-parity. Advanced motional Stark effect (MSE) spectroscopy diagnostics suggests a possible role of the reversed or flattened iota profile for the mode excitation and the ITB collapse [7].

(T. Kobayashi)

[1] H. Takahashi *et al*., Nucl. Fusion **58**, 106028 (2018).
[2] H. Takahashi *et al*., presented in the 22nd International Stellarator Heliotron Workshop, Madison, USA, I-2 (2019).
[3] K. Ogawa *et al*., Nucl. Fusion **58**, 044001 (2018).
[4] T. Kobayashi *et al*., Plasma Phys. Control. Fusion **61**, 085005 (2019).
[5] T. Kobayashi *et al*., Sci. Rep. **9**, 15913 (2019).
[6] H. Yamada *et al*., Phys. Rev. Lett. **123**, 185001 (2019).
[7] T. Kobayashi *et al*., Nucl. Fusion **60**, 036017 (2020).

Transport and Confinement

Highlight

Isotope effect on energy confinement and thermal transport in NBI-heated plasmas in LHD

It has been recognized that thermal transport in toroidal plasmas is dominated by the turbulence with the characteristic scale of ion gyro-radius. However, while this gyro-Bohm model predicts $\chi \propto \rho^* \propto M^{1/2}$, major experimental observations in tokamak have shown better confinement in deuterium(D) with heavier mass M than in hydrogen(H). This isotope effect remains a long-standing mystery in fusion research. Extensive and elaborated comparisons of H and D plasmas in LHD have unveiled the co-existence of the gyro-Bohm nature and significant mass dependence.

The regression analysis of thermal energy confinement time has shown $\tau_{E,th}^{scl} \propto M^{-0.02} B^{0.89} \bar{n}_e^{0.75} P_{abs}^{-0.90}$. Here no significant dependence on M is distinguished and this expression is inconsistent with the gyro-Bohm model suggesting $M^{-0.5}$ dependence. However, this scaling expression rephrased into the dimensionless form yields $\tau_{E,th}^{scl} \Omega_i \propto M^{0.98} \rho^{*-2.99} \nu^{*0.21} \beta^{-0.35}$. It should be noted that the gyro-Bohm nature is described as $\tau_E \Omega_i \propto M^0 \rho^{*-3}$. Additional clear M dependence is identified here, which compensates unfavorable negative dependence on M in the gyro-Bohm model while the gyro-Bohm dependence of ρ_*^{-3} persists.

Then thermal diffusivity in dimensionally similar plasmas has been compared. Since the three operational parameters B, $\bar{n}_e$, and P_{abs} are controllable in the experiment, dimensionally identical conditions in terms of ρ^*, ν^*, and β can be fulfilled for plasmas with different M [1]. Normalized thermal diffusivity χ/Ω_i is expected to be the same between these dimensionally similar plasmas. However, Fig. 1 shows that $\chi_e/(S_{2/3}\Omega_i)$ is improved robustly in D from H by a factor of around 2, which may implicate $1/M$. Therefore, reduction of thermal diffusivity in D is consistent with the significant mass dependence seen in the dimensionless expression of $\tau_{E,th}^{scl}$.

[1] H. Yamada *et al.*, Phys. Rev. Lett. **123**, 185001 (2019).

(H. Yamada, The University of Tokyo)

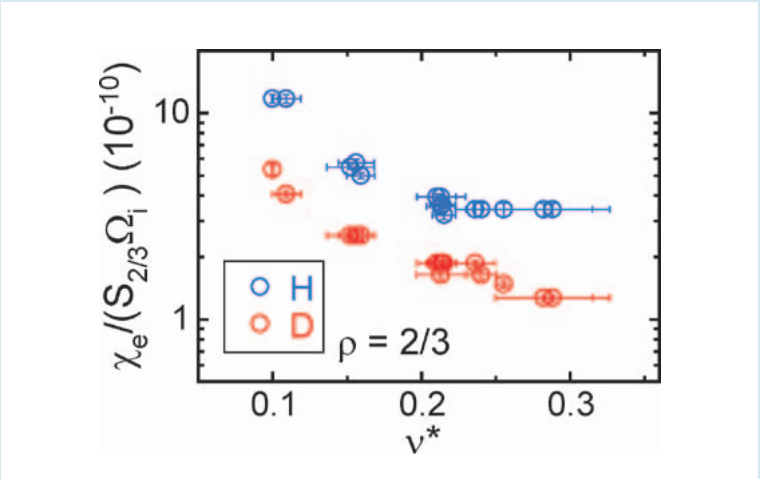

Fig. 1 Comparison of dimensionally similar plasmas. The thermal diffusivity at ρ=2/3 normalized by the corresponding surface area $S_{2/3}$ and Ω_i as a function of ν^*.

Isotope-mixing and non-mixing states in hydrogen-deuterium mixture plasmas

Transition between isotope-mixing and non-mixing states in hydrogen-deuterium mixture plasmas is observed in the isotope (hydrogen and deuterium) mixture plasma in LHD. In the non-mixing state, the isotope density ratio profile is non-uniform when the beam fueling isotope species differs from the recycling isotope species and the profile varies significantly depending on the ratio of the recycling isotope species. Bulk charge exchange spectroscopy system [1] has been installed in LHD to measure the radial profiles of hydrogen fraction $n_H/(n_H+n_D)$ in the plasma from H_α and D_α lines emitted by the charge exchange reaction between the bulk ions and the neutral beam injected. The transition from non-mixing state to isotope-mixing state is observed after H and D pellet injections [2]. Before the pellet injection the H density profile is much more peaked than the D density profiles due to the H beam fueling and D dominating recycling as seen in Fig. 1 (a), and the hydrogen fraction is non-uniform (isotope non-mixing state). After the pellet injection, the hydrogen fraction becomes uniform (isotope mixing state) as seen in Fig. 1 (b).

Figure 2 (a) (b) shows the density fluctuation spectrum integrated from edge to core along the laser beam line of the central chord of phase contrast imaging (PCI) for non-mixing and isotope-mixing states and the linear growth rates calculated with gyrokinetic simulation code GKV for TEM and ITG turbulence. The fast transition from non-mixing state to isotope-mixing state (nearly uniform profile of isotope ion density ratio) is observed associated with the change of electron density and its profile (with peaked with hollow) by the pellet injection near the plasma periphery. The transition from non-mixing to isotope-mixing state strongly correlates with the increase of turbulence and the transition of turbulent state from TEM to ITG mode as predicted by gyrokinetic simulation.

This results shows that non-mixing and the isotope-

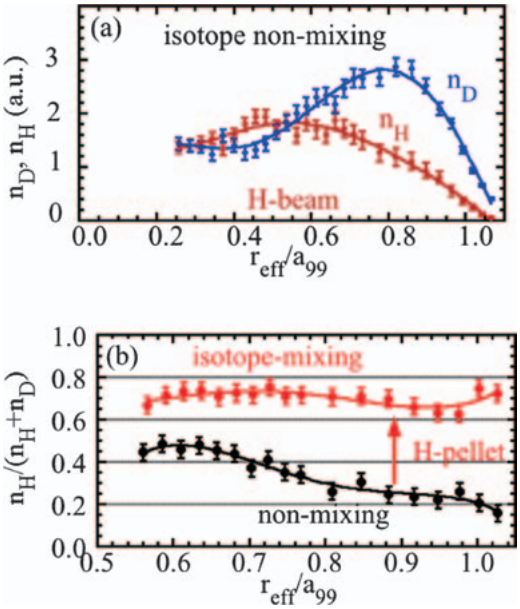

Fig. 1 Radial profiles of (a) hydrogen and deuterium density in isotope non-mixing state and (b) hydrogen fraction before and after the H-pellet injection.

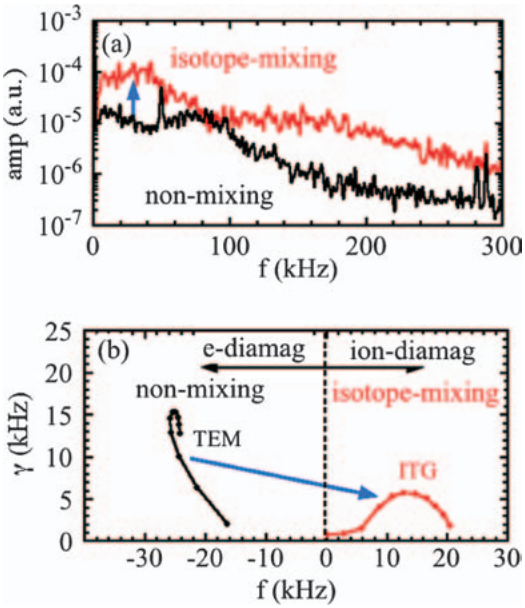

Fig. 2 (a) Density fluctuation spectrum measured with PCI and (b) the linear growth rate at r_{eff}/a_{99}=0.8 for the isotope non-mixing and mixing states calculated with GKV.

mixing states depend on the turbulent state and give the essential knowledge for predicting the isotope density profiles in the D-T mixture plasma in JET and ITER.

[1] K.Ida, *et.al.*, *Rev. Sci. Instrum.* **90**, (2019) 093503.
[2] K.Ida, *et.al.*, *Phys. Rev. Lett.* **124**, (2020) 025002.

(K. Ida)

Improved performance of ECRH by perpendicular injection [1]

Adjustments of launcher settings of electron cyclotron resonance heating (ECRH) are necessary to produce high-performance plasma. The precise evaluation of deposition profiles is also essential for transport studies. For such purposes, a method of perpendicular injection on the horizontally elongated cross section was developed to improve performance of ECRH in LHD. Perpendicular injection to the ECR layer can be more insensitive to the effect of refraction in comparison to the conventional oblique injection. However, the perpendicular injection had not been performed and the oblique injection had been standard in LHD. This is because the unabsorbed wave by perpendicular injection will damage divertor tiles and heat the cryo-sorption panel in closed divertors. Thus, the interlock system for gyrotron power output was developed to avoid injection to extremely low n_e plasma in which the EC wave is less absorbed.

Achieved T_e profiles were compared between the two kinds of injection of 1 MW without modulation. Plasmas were sustained by another two 154 GHz gyrotrons with 1 MW injection power each. As shown in Fig. 1, T_{e0} increased from 4 keV by the standard oblique injection up to 6 keV by the newly developed perpendicular injection at $n_{e,avg} = 1\times10^{19}$ m^{-3}. This will contribute to extending high T_i-T_e regime. Modulation ECRH experiments indicate that perpendicular injection shows better central heating than oblique injection. Refraction and Doppler-shifted absorption in oblique propagation of the EC wave cause broadening of the deposition profiles, in particular at high n_e.

Such an improved ECRH performance has opened up a new operational region in ECRH plasma. As shown in Figs. 2 (a1)~(d1), high density plasma of $n_{e0} \sim 8\times10^{19}$ m^{-3} was successfully sustained after injection of three consecutive hydrogen ice pellets for the first time only by ECRH in LHD. Two 154-GHz gyrotrons for standard oblique injection and one 77-GHz gyrotron for perpendicular injection were used for plasma sustainment. Hollow n_e profiles by

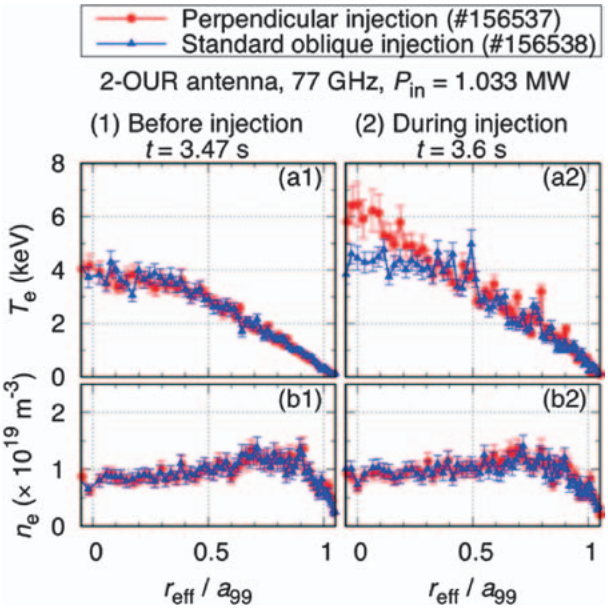

Fig. 1 Comparisons of radial profiles of (a) T_e and (b) n_e (1) before and (2) during perpendicular/oblique injection [1].

gas puffing changed to rather peaked profiles after the pellet injection. Equipartition heating was significant in the high-n_e region: $T_{i0} \sim T_{e0} \sim 1$ keV at $n_{e0} \sim 8\times10^{19}$ m^{-3} and $T_{i0} \sim T_{e0} \sim 2$ keV at $n_{e0} \sim 5\times10^{19}$ m^{-3} were achieved. τ_E at the W_p peak is estimated to be 0.2 s. On the other hand, in the case of oblique injection for the 77-GHz ECRH, high n_e plasma was radiatively collapsed due to the increase of radiation, as shown in Figs. 2 (a2)~(d2). Accumulated database of high n_e discharges with a wide range of n_e by perpendicular injection of higher P_{ECRH} will contribute to comparative studies between different devices such as W7-X, as well as for isotope effect studies.

[1] T. Ii Tsujimura *et al.*, Nucl. Fusion to be submitted.

(T. Tsujimura)

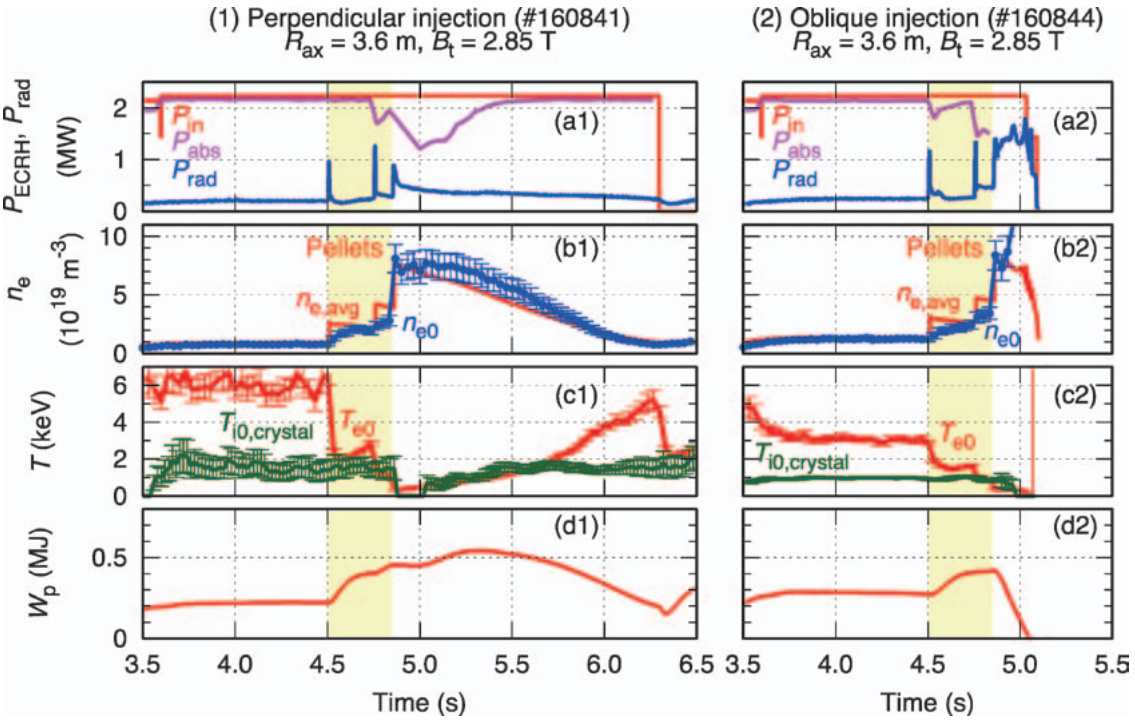

Fig. 2 Comparisons of time evolution of (a) injection power P_{in} and absorption power P_{abs} of ECRH, radiation power P_{rad}, (b) n_{e0}, $n_{e,avg}$, (c) T_{e0}, T_{i0} measured with the crystal spectrometer, and (d) W_p between (1) perpendicular injection and (2) oblique injection [1].

Edge/Divertor/Atomic and Molecular Processes

Highlight

The Impurity Powder Dropper was installed and employed in dedicated experiments

Wall conditioning techniques with low-Z impurities such as boron (B) or lithium are fundamental for accessing low collisionality plasmas, and are employed routinely on tokamaks and stellarators. The Impurity Powder Dropper (IPD), designed and built by PPPL, allows the injecting of low-Z impurities in the form of sub-millimeter powder grains into the plasma, potentially performing a real-time wall-conditioning of the plasma facing components, without interruption of plasma operation.

To investigate the viability of this technique in steady-state operation, the IPD has been installed in LHD sector 2.5 (Fig. 1). A first series of dedicated experiments has been performed, where controlled amounts of B and boron nitride (BN) powder have been injected in a variety of plasma conditions, featuring different species (H and He), heating schemes and magnetic configurations, in discharges of a duration ranging from 4 seconds to 9 minutes.

The successful injection of the powder grains into the plasma is confirmed by multiple diagnostics, such as visible cameras (Fig. 2), UV and charge exchange spectroscopy. Preliminary results show a reduction of wall fueling both on a shot-to-shot basis and even in real time for longer discharges. The intrinsic level of impurities (oxygen and carbon) was also observed to decrease after cumulative injection of B, when the powder injection was performed in the absence of a standard glow discharge boronization.

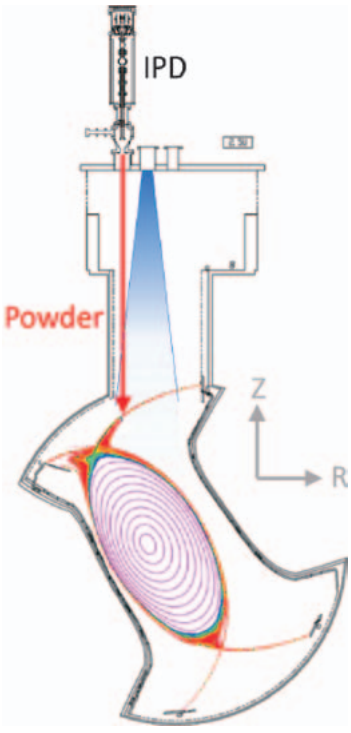

Fig. 1 Position of the IPD on the LHD vacuum vessel with the corresponding plasma poloidal cross section, and field of view of the visible camera.

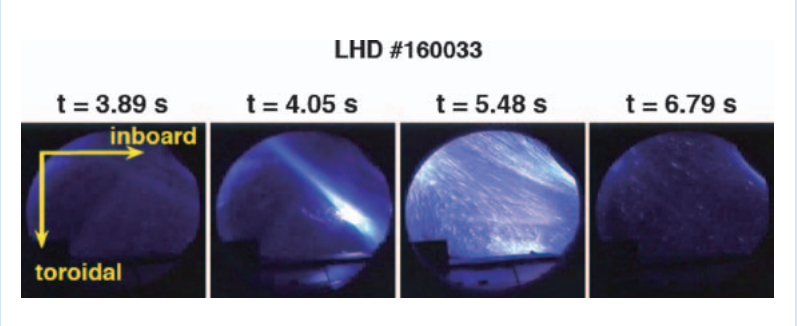

Fig. 2 Visible camera imaging of boron powder injection in LHD plasma.

Steady-state sustainment of divertor heat load reduction with multi-species impurity seeding in LHD

To manage the power exhaust in fusion reactors, a radiation enhancement is required not only in the divertor region but also in the upstream region with suppression of dilution and contamination. Multi-species impurity seeding is a candidate to realize the radiation enhancement in the edge plasma region, and divertor heat load reduction.

Superimposed seeding of higher-Z (Kr) and lower-Z (Ne) impurities have been applied to the LHD plasma [1]. As shown in Fig. 1, although reduction of divertor heat flux, q_{div}, is not significant after Kr seeding at 4.1 s, q_{div} decreases by ~ 85% after Ne seeding at 4.5 s. While the q_{div} reduction only using Ne seeding disappears 0.4 s after the seeding, the q_{div} reduction in Kr+Ne seeded plasma can be sustained for 1 s until termination of NBI heating. T_e decreases at $|r_{eff}/a_{99}| > 0.8$ due to the Ne seeding as shown in Fig. 2 (b). The T_e reduction enhances the emission from the pre-seeded Kr. Negative E_r is formed in the edge plasma and sustained until termination of deuterium gas puff. The negative E_r should be a key for the enhancement of the Kr emission and the sustainment of the heat load reduction. As shown in Fig. 2 (c), the radiation profile in the Kr+Ne seeded plasma can be shifted to upstream region compared with the profile of the only Ne seeded plasma with the same radiation fraction. These results indicate the availability of multi-species impurity seeding with different cooling rate.

[1] K. Mukai *et al.*, Plasma Fusion Res. **15**, 1402051 (2020).

(K. Mukai)

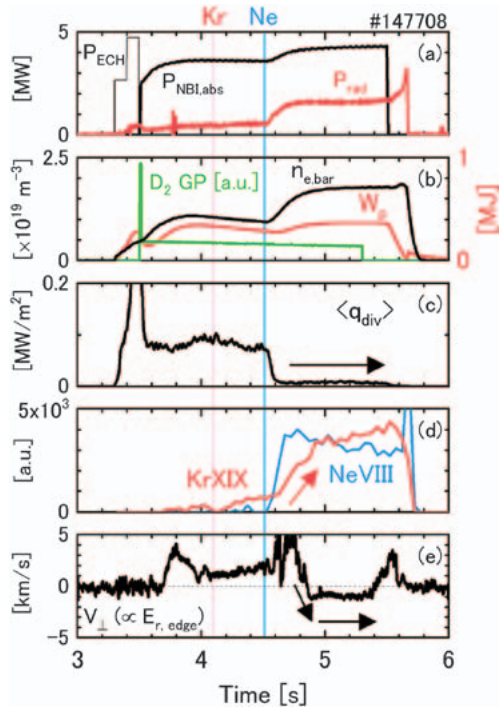

Fig. 1 Waveform of Kr+Ne seeded plasma in LHD. (a) Heating power and plasma radiation power, (b) line-averaged electron density, deuterium gaspuff, and plasma stored energy, (c) divertor heat flux, (d) Line emission of NeVII and KrXIX, and (e) radial electric field at edge plasma.

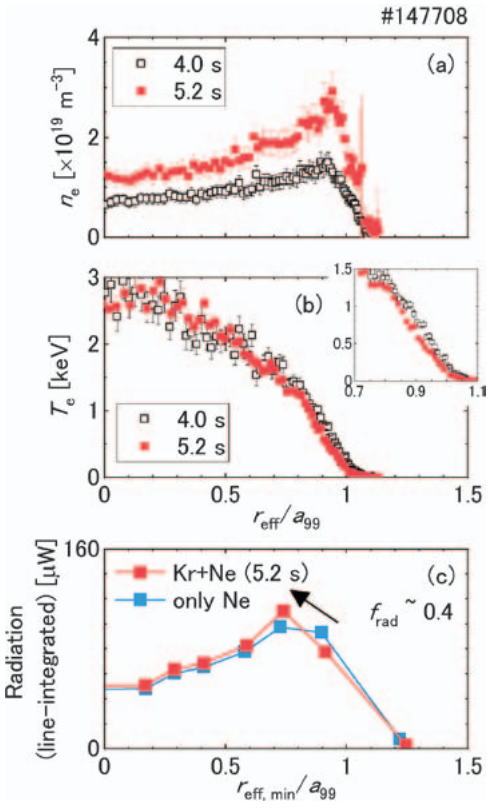

Fig. 2 Radial profiles of Kr+Ne seeded plasma in LHD. (a) electron density, (b) electron temperature, and (c) plasma radiation.

Multi-wavelength spectroscopic observation of line emissions from tungsten ions with a wide range of charge states

Spectroscopic studies for emissions released from tungsten (W) ions ranging from low to high charge states have been intensively conducted in LHD for contribution to the impurity transport study in fusion devices with plasma facing components made of W such as ITER and DEMO, and for the expansion of experimental database of W line emissions. In order to observe the line emissions released from W ions efficiently, W ions are distributed in the LHD plasma by injecting a pellet consisting of a small piece of W metal wire enclosed by a carbon tube. Figure 1 shows ionization energy of W ions, E_i, as a function of charge state, q^+. Ranges of the electron temperature, T_e, of the ITER core plasmas and the LHD core plasmas with W pellet injection are illustrated together for a rough guideline of the distribution of charge states. As shown in the figure, from the neutral atoms, W^0, to the highly-ionized ions up to W^{45+} are observed simultaneously by applying the spectroscopic diagnostics for extreme-ultraviolet (EUV), vacuum-ultraviolet (VUV), and visible wavelength ranges. Figure 2 shows a typical waveform of the W pellet injection experiment in LHD. After the tungsten pellet injection at 4.1 s, the central electron temperature, T_{e0}, once decreases, and then T_{e0} recovered up to around 3 keV by a superposition of ECH for 4.2~4.7 s. At 5.3 s, T_{e0} decreases down to the minimum value with switching the NBIs from the negative ion-sourced NBI (n-NBI) to the positive ion-sourced NBI (p-NBI). In the low T_{e0} phase, the T_e profile is extremely hollow, the so-called "temperature hole" [1]. Even though T_{e0} becomes close to zero, finite value of low T_e is distributed within the confinement region, so it is still possible for W ions to be distributed with releasing emissions. Figure 3 shows wavelength spectra including W line emissions observed in high T_{e0} (= 2.7 keV) and low T_{e0} (~0 keV) phases, which were obtained in the red and blue-hatched periods in Fig. 2, respectively. As shown in Fig. 3 (a-c), W^{41+}, W^{42+}, W^{43+}, W^{45+} lines and W^{24+} ~ W^{33+} ,W^{24+} ~ W^{29+} unresolved-transition arrays (UTAs) are observed in the EUV range as well as the magnetic dipole forbidden transitions of W^{26+} and W^{27+} in the visible range are observed in the high T_{e0} phase [2,3]. On the other hand, W^{6+} and W^{5+} lines are observed in the EUV and VUV ranges, respectively, in the low T_{e0} phase as shown in Fig. 3 (d, e) [4]. Thus, variation in the dominant charge states of W ions against T_{e0} has been successfully demonstrated in a single discharge. This observation can contribute as a fundamental dataset for evaluation of W concentration in the plasmas even in the cases that W ions are sputtered from the plasma facing components.

[1] C. Suzuki *et al.*, Plasma Phys. Control. Fusion **59**, 014009 (2017).
[2] Y. Liu *et al.*, Plasma Fusion Res. **13**, 3402020 (2018).
[3] S. Morita *et al.*, Journal of Physics: Conf. Series **1289**, 012005 (2019).
[4] T. Oishi *et al.*, Phys. Scr. **91**, 025602 (2016).

(T. Oishi)

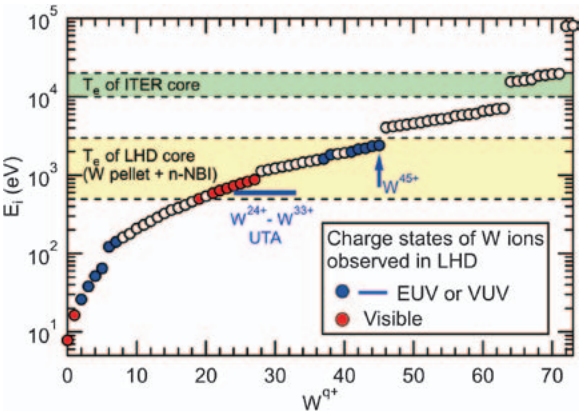

Fig. 1 Ionization energy, E_i, of W ions as a function of charge state, q^+. Green and yellow-hatched regions indicate electron temperature range at $T_e = E_i$ for ITER core plasmas and LHD core plasmas with W pellet injection, respectively.

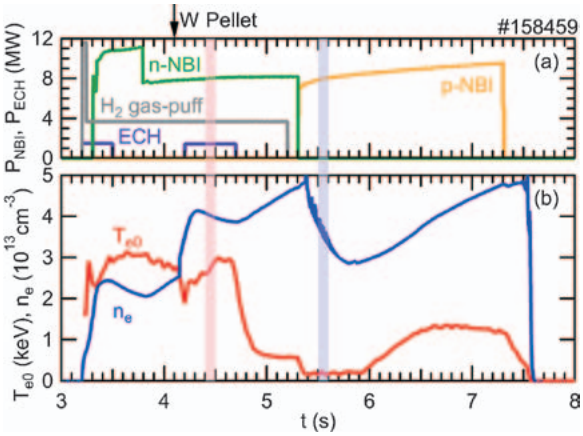

Fig. 2 Typical waveform of the W pellet injection experiment in LHD. (a) Injection power of NBI and ECH and (b) central electron temperature, T_{e0}, and line-averaged electron density, n_e.

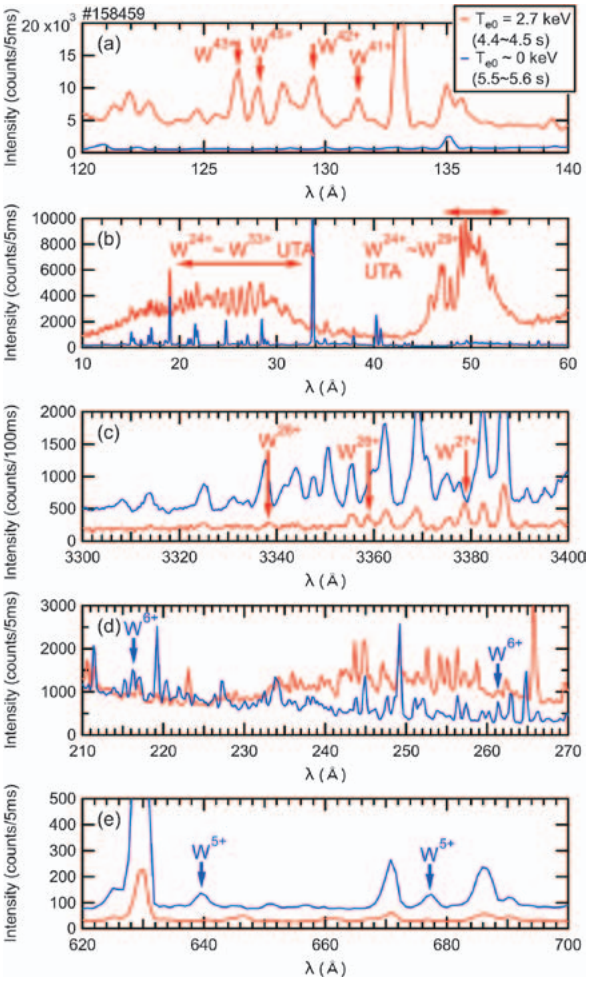

Fig. 3 Wavelength spectra including line emissions released from W ions observed in high T_{e0} (= 2.7 keV) and low T_{e0} (~0 keV) phases. (a) W^{41+}, W^{42+}, W^{43+}, W^{45+} lines, (b) W^{24+} ~ W^{33+} and W^{24+} ~ W^{29+} UTAs in the EUV range and (c) the magnetic dipole forbidden transitions of W^{26+} and W^{27+} in the visible range are observed in the high T_{e0} phase. (d) W^{6+} lines in EUV range and (e) W^{5+} lines in VUV range are observed in the low T_{e0} phase.

High-beta/MHD/Energetic Particles

Highlight

High-beta plasma production examined in Deuterium experiment

An aim of the LHD project is the realization of the reactor-relevant high-beta plasma, where the volume averaged beta, $\langle\beta\rangle$, is 5%, at B = 1~2 T. In the hydrogen experiment before the 19th campaign, the beta value achieved 3.4% and 4.1%, which are the quasi-steady state by the gas puffing and the transient by the pellet injection, respectively. However, in the deuterium experiment, due to the power degradation of the tangential NBI, the plasma start-up in the low field was impossible. For solving that problem, in the 21st campaign, only one tangential NBI keeps the hydrogen operation for expecting the high heating power. Then the high-beta production examined comparing with the hydrogen plasma.

Figure 1 shows the dependency of the achieved beta value on the line averaged density. The circle symbol indicates the quasi-steady state discharge by the gas puffing, and the triangle symbol indicates the transient discharge by the pellet injection. The color indicates the pre-set vacuum magnetic axis. For both quasi-steady state and transient discharges, the highest beta values were achieved at R_{ax} = 3.55 m. For discharges of the gas puffing, it seems the degradation due to the increased density, but for the pellet injection, there is no degradation by the increased density. The fine-tuning of the density is the next step.

(Y. Suzuki)

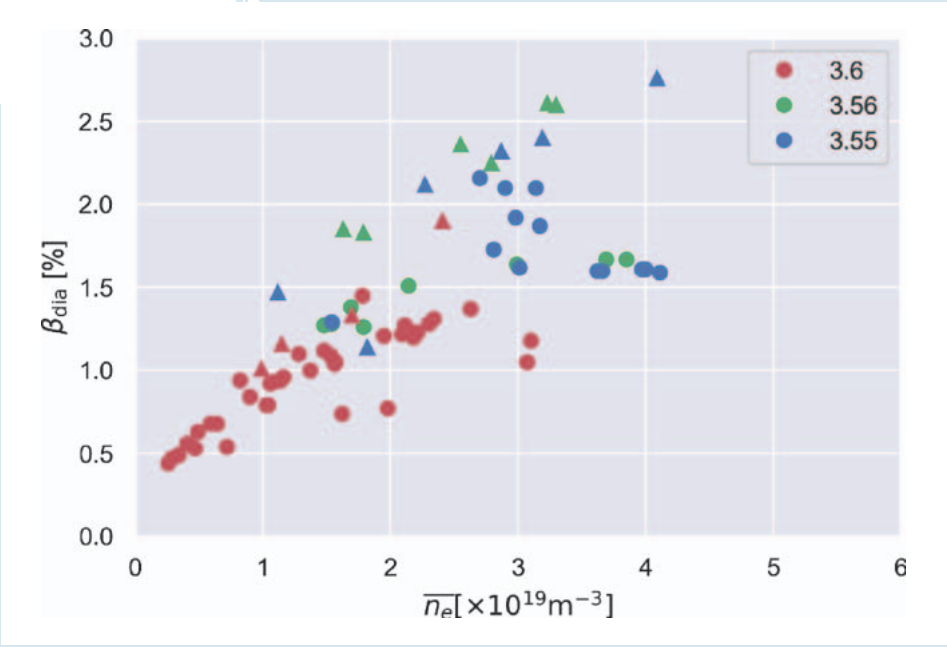

Fig. 1 the dependency of the achieved beta value on the line averaged density.

Energetic Particle Transport by Helically-trapped Energetic-ion-driven Resistive Interchange Mode in LHD

In high-ion temperature experiment performed in relatively low-density plasma with intense positive-ion-source based perpendicular neutral beam injections (P-NBI) in the Large Helical Device (LHD), the helically-trapped energetic-ion-driven resistive interchange mode (EIC) is often observed [1,2] and limits sustainment of the high-ion-temperature state [3]. To sustain the high-ion-temperature state for a longer period, a study of energetic ion transport due to EIC was performed using neutron diagnostics in LHD [4].

We used two vertical neutron cameras (VNCs) to measure the time evolution of the neutron profile. VNC1 [5] characterized by a high spatial resolution based on stilbene fast-neutron detector and VNC2 characterized by high detection efficiency based on EJ410 fast-neutron scintillator were installed under the floor concrete of the torus hall. VNC1 and VNC2 were installed in the vertical elongated poloidal cross section and the diagonal poloidal cross section, respectively. Figure 2 shows the typical density profile of helically-trapped beam ion created by P-NB injection in relatively low-density plasma calculated by MORH code [6] with sightlines of VNCs.

Figure 3 shows line-integrated neutron profiles measured by VNC1 and VNC2 before and after the EIC burst.

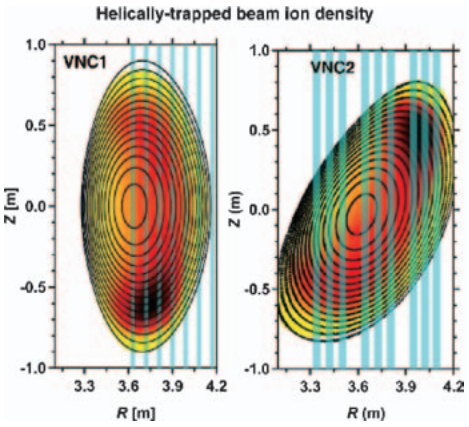

Fig. 2 Helically trapped beam ion density created by P-NB injection and sight lines of VNCs.

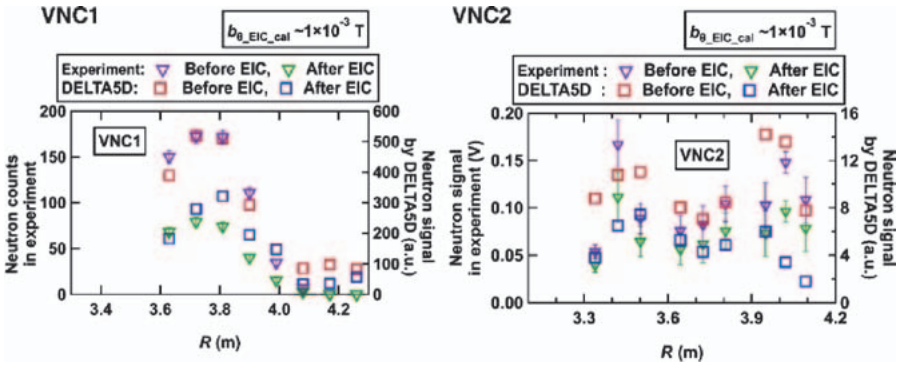

Fig. 3 Line-integrated neutron profile before and after the EIC burst.

Here, the neutron counts measured by VNC1 at a time interval of 20 ms and the averaged signals over 20 ms measured by VNC2 are plotted. These results showed that the neutron profiles were substantially changed due to the EIC burst. Guiding-center orbit-following simulations, including EIC fluctuations, were performed to understand the helically-trapped beam ion transport due to EIC. A comparison of the line-integrated neutron profile before and after the EIC burst measured in the experiment and obtained by the numerical simulation is shown in Fig. 3. The neutron profile for VNC1 shows a single peak appeared at R of approximately 3.75 m, which is nearly equal to the peak position measured in the experiment. The neutron counts for VNC1 at the central channel (R from 3.6 m to 3.9 m) becomes almost one-half after the EIC burst, as measured in the experiment. Although there are relatively wide peaks for line-integrated neutron profile for VNC2 compared with the experiment, the neutron signal shows two peaks in numerical calculation. A decrease in the neutron signal due to the EIC burst at two peaks corresponding to helical ripple valley is reproduced.

[1] Du X. D. *et al.*, 2015 Phys. Rev. Lett. **114**, 155003.
[2] Du X. D. *et al.*, 2015 Nucl. Fusion **56**, 016002.
[3] Takahashi H. *et al.*, 2018 Nucl. Fusion **58**, 106028.
[4] Isobe M. *et al.*, 2018 IEEE Trans. Plasma Sci. **46**, 2050.
[5] Ogawa K. *et al.*, 2018 Rev. Sci. Instrum. **89**, 113509.
[6] Seki R. *et al.*, 2015 Plasma Fusion Res. **10**, 1402077.

(K. Ogawa)

Observation of the Transported Particles Using an Upgraded Neutral Particle Analyzer during TAE Burst in the Large Helical Device

The bursting toroidal Alfvèn eigenmodes (TAEs) [1] are often observed in relatively low magnetic field experiments in the Large Helical Device (LHD). In previous studies, by measuring the transported neutral particles by the TAE burst using the E-parallel-B type neutral particle analyzer (E‖B-NPA) [2] and using the lost ion using scintillator-based fast-ion loss detector (FILD), the existence of the hole-clump pairs was suggested in real space [3–5]. To measure the time evolution of the energetic particles transported by TAE bursts in more detail, the E‖B-NPA was upgraded. The time duration of the observed single TAE burst is approximately 0.5 ms with the frequency chirping down. Therefore, the measurement time resolution is important for measuring the detailed structure of the transported energetic particles during the TAE burst. The measurement electronic circuits of the E‖B-NPA were updated, and the time resolution was improved up to 100 kilo samples per second [6].

During the tangential neutral beam (t-NB) #1 injection in the magnetic field at the magnetic axis is 0.6 T, TAE bursts were observed by the Mirnov coils and the E‖B-NPA. Figure 4 shows the (a) signal of the Mirnov coil, (b) the spectrogram of the magnetic fluctuations, and (c) the energy spectrum of the particle flux Γ observed by E‖B-NPA. The TAE bursts were observed with the time intervals of approximately 10 ms. During and after the TAE bursts, the transported particles were observed by E‖B-NPA. Figure 5 shows the result of the conditional averaging technique for the amplitude of the magnetic fluctuation and the changing of the observed particle flux $\Delta\Gamma$ measured by E‖B-NPA with using 72 TAE bursts. The peak amplitude of the magnetic fluctuation of 70 kHz is set to 2.0 ms. By the conditional averaging technique, the structure of the transported particles is clearly con-

firmed during and after the TAE burst. The highest detected energy of the transported particles is 150 keV, which is less than the injection beam energy of 180 keV. The energy slowing down time was 1.0–1.5 ms during the TAE burst, and 6–8 ms after the TAE burst. The energy slowing down during the TAE burst is considered to be related to the TAE burst frequency chirping down, and the energy slowing down after the TAE burst can be considered as the classical energy slowing down time.

[1] Cheng C. Z. and Chance M. S. 1986 Phys. Fluids **29**, 3695.
[2] Medley S. S. and Roquemore A. L. 1998 Rev. Sci. Instrum. **69**, 2651.
[3] Osakabe M. *et al.*, 2006 Nucl. Fusion **46**, S911-S917.
[4] Ogawa K. *et al.*, 2009 J. Plasma Fusion Res. SERIES **8**, 655.
[5] Ogawa K. *et al.*, 2010 Nucl. Fusion **50**, 084005.
[6] Fujiwara Y. *et al.*, 2020 JINST **15**, C02021.

(S. Kamio)

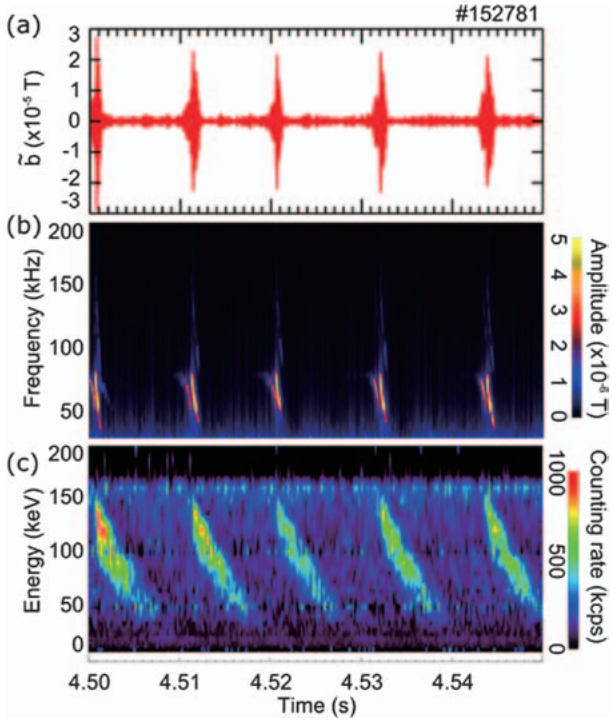

Fig. 4 Time evolutions of (a) the signal of the Mirov coil, (b) the spectrogram of the magnetic fluctuations, and (c) the energy spectrum of the particle flux Γ observed by E||B-NPA.

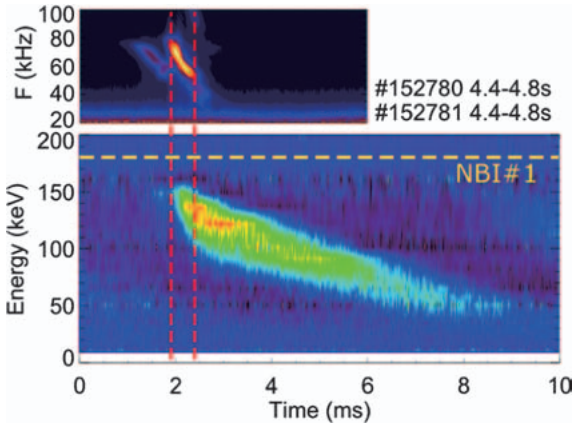

Fig. 5 The conditional averaged spectrogram of the magnetic fluctuation and the ΔΓ observed by E||B-NPA. Red dashed lines are the timing of the start and the end of the TAE bursts. Yellow dashed line is the injection energy of the NB #1.